Metallomics, 14, 2022, mfac068
https://doi.org/10.1093/mtomcs/mfac068
Advance access publication date: 8 September 2022
Paper

Lysosome-targeted cyclometalated iridium(III) complexes: JMJD inhibition, dual induction of apoptosis, and autophagy

Jun-Jian Lu[1,‡], Xiu-Rong Ma[1,‡], Kai Xie[1], Mei-Ru Chen[1], Bo Huang[2,*], Rong-Tao Li[1,*] and Rui-Rong Ye[1,*]

[1]Faculty of Life Science and Technology, Kunming University of Science and Technology, Kunming 650500, P. R. China and [2]Faculty of Chemistry and Chemical Engineering, Yunnan Normal University, Kunming 650500, P. R. China
*Correspondence: Yunnan Normal University, No. 1, Yuhua, Chenggong District, Kunming 650500, Yunnan, P. R. China. E-mail: huangbo15@foxmail.com (Bo Huang); Kunming University of Science and Technology, No. 727, South Jingming Road, Kunming 650500, Yunnan, P. R. China. E-mail: rongtaolikm@163.com (Rong-Tao Li); E-mail: yerr@mail2.sysu.edu.cn (Rui-Rong Ye)
‡These authors contributed equally.

Abstract

A series of cyclometalated iridium(III) complexes with the formula $[Ir(C^N)_2 L](PF_6)$ (C^N = 2-phenylpyridine (ppy, in **Ir-1**), 2-(2-thienyl)pyridine (thpy, in **Ir-2**), 2-(2,4-difluorophenyl)pyridine (dfppy, in **Ir-3**), **L** = 2-(1H-imidazo[4,5-f][1,10]phenanthrolin-2-yl)quinolin-8-ol) were designed and synthesized, which utilize 8-hydroxyquinoline derivative as N^N ligands to chelate the cofactor Fe^{2+} of the Jumonji domain-containing protein (JMJD) histone demethylase. As expected, the results of UV/Vis titration analysis confirm the chelating capabilities of **Ir-1–3** for Fe^{2+}, and molecular docking studies also show that **Ir-1–3** can interact with the active pocket of JMJD protein, and treatment of cells with **Ir-1–3** results in significant upregulation of trimethylated histone 3 lysine 9 (H3K9Me3), indicating the inhibition of JMJD activity. Meanwhile, **Ir-1–3** exhibit much higher cytotoxicity against the tested tumor cell lines compared with the clinical chemotherapeutic agent cisplatin. And **Ir-1–3** can block the cell cycle at the G2/M phase and inhibit cell migration and colony formation. Further studies show that **Ir-1–3** can specifically accumulate in lysosomes, damage the integrity of lysosomes, and induce apoptosis and autophagy. Reduction of mitochondrial membrane potential and elevation of reactive oxygen species also contribute to the antitumor effects of **Ir-1–3**. Finally, **Ir-1** can inhibit tumor growth effectively *in vivo* and increase the expression of H3K9Me3 in tumor tissues. Our study demonstrates that these iridium(III) complexes are promising anticancer agents with multiple functions, including the inhibition of JMJD and induction of apoptosis and autophagy.

Keywords: cyclometalated iridium(III) complexes, lysosome-targeted, 8-hydroxyquinoline, JMJD inhibition, apoptosis, autophagy

Graphical abstract

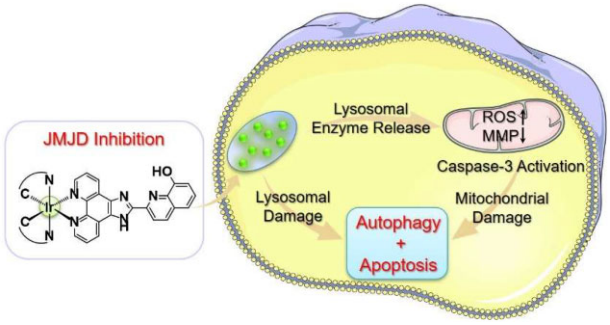

Lysosome-targeted cyclometalated iridium(III) complexes exhibit multiple functions, including inhibition of JMJD and induction of apoptosis and autophagy.

Introduction

The clinical success of platinum-based drugs has stimulated a strong interest in finding other metal-based anticancer drugs.[1,2] Many non-platinum anticancer drugs exhibit better antitumor activity and lower side effects through mechanisms of action different from those of platinum drugs.[3–5] Among them, cyclometalated iridium(III) complexes have emerged as promising alternatives to platinum-based drugs because they possess multiple anticancer modes, including perturbing the redox status of cells,[6–9]

Received: July 3, 2022. **Accepted:** August 28, 2022

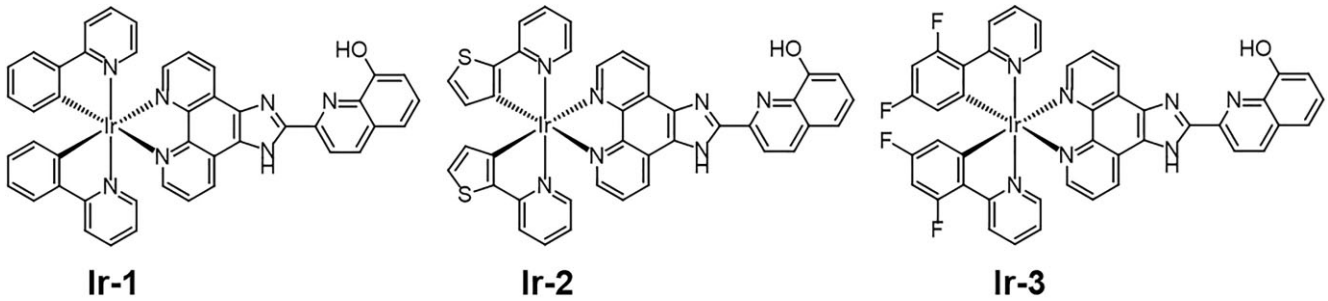

Scheme 1. Chemical structures of **Ir-1–3**.

damaging specific subcellular organelles[10–13] and inhibiting enzyme activities,[14–16] and these antitumor modes can work together synergistically to improve the efficacy of the drug.[17–19] Meanwhile, Jumonji domain-containing protein (JMJD) histone demethylases are important epigenetic regulators in cancer cells. Various studies have shown that JMJD histone demethylases are overexpressed in a variety of cancer cells, including breast cancer, colorectal cancer, lung cancer, prostate cancer, etc., which is the main culprit of cancer cell proliferation, metastasis, and drug resistance.[20–25] Drug design targeting JMJD histone demethylase is also a focus of current antitumor drug development.[26–31] Among them, only one case of organometallic iridium complex with JMJD inhibitory activity has been reported so far, which can effectively inhibit cell proliferation and induce apoptosis.[17]

Lysosomes (pH: 4.5–5.5) are cellular waste disposal units that contain different types of hydrolytic enzymes capable of degrading almost all kinds of biomolecules in cells.[32,33] Disruption of the lysosomal integrity, a process known as lysosomal membrane permeabilization (LMP), can cause the release of lysosomal components, such as cathepsins and other hydrolases, from the lysosomal lumen to the cytosol.[34] And the cathepsins and other hydrolases initiate a cascade of biological events, including substrate degradation, caspase activation, and reduction of mitochondrial membrane potential (MMP), eventually leading to cell death.[35] As a result, the antitumor drugs that can facilitate LMP are worth designing and developing. For example, Liu *et al.* reported a series of half-sandwich iridium(III) complexes and ruthenium(II) complexes that targeted the lysosome, disrupted the lysosomal integrity, increased intracellular reactive oxygen species (ROS) levels, and decreased MMP, ultimately induced the activation of the mitochondrial apoptotic pathway.[36,37] Recently, Chao *et al.* prepared a ruthenium complex with near-infrared absorption for photodynamic therapy, which could induce cell apoptosis by generating singlet oxygen and damaging lysosomes.[38]

Damaging lysosomes may induce programmed cell death (RCD), including apoptosis, autophagy, and ferroptosis.[39] RCD is a physiological and active 'conscious suicide' of cells, which plays an important role in organismal development, homeostasis, and pathogenesis.[40] Apoptosis, the most common form of RCD, can be initiated through death receptors on the cell surface (extrinsic pathway) or through mitochondria (intrinsic pathway), ultimately leading to the activation of an initiator caspase.[41,42] In tumor treatment, most chemotherapeutic drugs exert their efficacy by inducing apoptosis in cancer cells.[43] Besides, autophagy as a common form of RCD is a lysosomal degradation pathway, which can induce autophagic death of cancer cells.[44,45] A growing number of studies have shown that the induction of multiple antitumor mechanisms can improve antitumor efficacy more efficiently.[13,36,46–48] Mao *et al.* reported that lysosome-targeted cyclometalated iridium(III) complexes could mediate both apoptosis and autophagy, and exhibited excellent anticancer activity *in vitro* and *in vivo*.[49]

Herein, we designed and synthesized a series of cyclometalated iridium(III) complexes with the formula $[Ir(C^N)_2\,\mathbf{L}](PF_6)$ (C^N = 2-phenylpyridine (ppy, in **Ir-1**), 2-(2-thienyl)pyridine (thpy, in **Ir-2**), 2-(2,4-difluorophenyl)pyridine (dfppy, in **Ir-3**), **L** = 2-(1H-imidazo[4,5-f][1,10]phenanthrolin-2-yl)quinolin-8-ol; Scheme 1), which utilize 8-hydroxyquinoline derivative as N^N ligands to chelate the cofactor Fe^{2+} of JMJD histone demethylase. First, the inhibitory ability of **Ir-1–3** on JMJD histone demethylase was confirmed by exploring their binding to Fe^{2+} using UV/Vis titration, molecular docking, and analyzing their effects on trimethylated histone 3 lysine 9 (H3K9Me3) expression levels. Next, we accessed the antiproliferative activity of **Ir-1–3** against the tumor cells. Besides, the anticancer mechanisms including cell cycle arrest, inhibition of cell migration and colony formation, cellular localization, cellular uptake mechanisms, lysosomal damage, induction of apoptosis and autophagy, mitochondrial damage, and intracellular ROS levels were elucidated. Finally, the antitumor activity of **Ir-1** *in vivo* was also evaluated. The results manifest that the cyclometalated iridium(III) complexes **Ir-1–3** are promising anticancer agents with multiple functions, including the inhibition of JMJD and induction of apoptosis and autophagy.

Results and discussion

Synthesis and photophysical characterization

The intermediate compounds $[Ir(C^N)_2$(5,6-diamino-1,10-phenanthroline)$](PF_6)$ were synthesized following literature methods.[50] Target compounds **Ir-1–3** were obtained by heating $[Ir(C^N)_2$(5,6-diamino-1,10-phenanthroline)$](PF_6)$ and 8-hydroxy-2-quinolinecarboxaldehyde in methanol for 24 h, followed by anion exchange with NH_4PF_6 (Scheme S1). They were then purified by column chromatography on silica gel using CH_2Cl_2/CH_3OH (30:1, v/v) as the eluent and characterized using ESI-MS (Figs. S1–S3), ^1H NMR (Figs. S4–S6), and elemental analysis.

The UV/Vis absorption spectra of **Ir-1–3** in PBS, CH_3CN, and CH_2Cl_2 were investigated at 298 K (Fig. S7A). In the UV region, **Ir-1–3** displayed intense absorption bands at ~250–420 nm originated from intraligand $\pi\rightarrow\pi^*$ transitions (^{1}LC). The relatively weak bands at ~420–510 nm were attributed to metal-to-ligand charge-transfer absorption. **Ir-1–3** exhibited green to orange phosphorescent emission upon excitation at 405 nm (Fig. S7B). And the emission intensity of **Ir-1–3** was very sensitive to solvent polarity. They were weakly emissive in PBS. However, the emission intensity was significantly enhanced in the nonpolar solvent CH_2Cl_2. The photophysical data of **Ir-1–3** are summarized in Table S1.

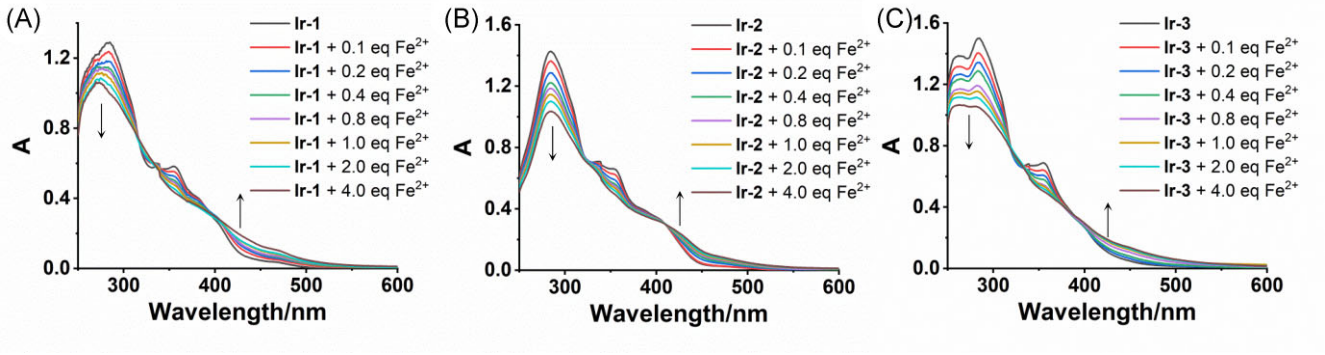

Fig. 1 UV/Vis spectra (2×10^{-5} M) of **Ir-1** (A), **Ir-2** (B), and **Ir-3** (C) upon addition of Fe^{2+} in H_2O/DMSO (1:1, v/v) at 298 K.

Binding of Ir-1–3 with Fe^{2+}

As Fe^{2+} is an essential cofactor of the JMJD proteins, the possibility that **Ir-1–3** could sequestrate Fe^{2+} to inhibit JMJD histone demethylase activity was investigated by UV/Vis absorption spectra.[51,52] As shown in Fig. 1, with the titration of Fe^{2+}, the absorption of **Ir-1–3** at 290–405 nm decreased, accompanied by an increase of the absorption at 405–430 nm. An isosbestic point was formed at around 405 nm, which indicated the formation of the new species upon the addition of Fe^{2+}. Besides, iron shuttles between the ferrous and ferric forms in the cell,[53] and the changes in UV/Vis absorption spectra of **Ir-1–3** in the presence of Fe^{3+} were also investigated (Fig. S8). In the presence of Fe^{3+}, the absorption of **Ir-1–3** underwent the same change phenomenon as Fe^{2+}. These results suggest that **Ir-1–3** can effectively chelate not only Fe^{2+} but also Fe^{3+}.

Molecular docking studies

In order to investigate the bonding mode and bonding mechanism between **Ir-1–3** and JMJD more intuitively, a molecular docking calculation was conducted. As shown in Fig. 2A, the terminal benzene ring on N^N ligand **L** of **Ir-1–3** could insert the pocket of JMJD (PDB code: 5ANQ) and interact with the active center Fe^{2+} through Fe^{2+}–π interaction. Meantime, the hydroxyl oxygen in the terminal benzene could coordinate with Fe^{2+}. On the other hand, the $Ir(C^N)_2$ moiety with the large steric hindrance of octahedral geometry could be firmly stuck outside the pocket, blocking the exit of the cavity of JMJD. As a result, the substrate of JMJD could not enter the pocket, serving to inhibit the JMJD activity. In addition, the bottom of the active pocket of JMJD was a negatively charged region, and **Ir-1–3** were positively charged ions, resulting in an electrostatic matching of the two, which improves the binding stability.

Based on the energy analysis, the binding energies of **Ir-1–3** and JMJD were –4.93, –4.95, and –4.89 kcal/mol, respectively. Because the binding modes and the interactions between **Ir-1–3** and JMJD were basically similar, the binding energies were also similar. In conclusion, **Ir-1–3** showed a good binding ability to JMJD and could be used to inhibit the demethylation activity of JMJD.

Upregulation of the histone-methylation level

JMJD can lead to the downregulation of H3K9Me3 and oncogene activation, thus the expression levels of H3K9Me3 can be used to monitor the activity of JMJD.[22,25] To further validate the ability of **Ir-1–3** to inhibit JMJD, we examined their effects on H3K9Me3 expression levels in human cervical cancer (HeLa) cells by Western blot. As shown in Fig. 3, the protein expression levels of H3K9Me3 significantly increased in a dose-dependent manner upon treatment of HeLa cells with **Ir-1–3**. The result suggests that **Ir-1–3** can inhibit the activity of JMJD.

Lipophilicity and *in vitro* cytotoxicity

Lipophilicity (log $P_{o/w}$) can affect the cellular uptake, distribution, and cytotoxicity of metal-based complexes.[54] Using a flask-shaking method, the log $P_{o/w}$ values of **Ir-1–3** were determined as follows: **Ir-3** (3.00) > **Ir-2** (2.99) > **Ir-1** (2.79). In addition, iridium is not an endogenous component of cells, therefore the cellular uptake efficiency of iridium can be quantitatively determined using inductively coupled plasma mass spectrometry (ICP-MS) analysis.[15] Upon incubation with 20 μM **Ir-1–3** for 2.5 h, the intracellular iridium contents of the compounds were in the following order: **Ir-2** (948.54 ng/10^6 cells) > **Ir-1** (786.00 ng/10^6 cells) > **Ir-3** (721.66 ng/10^6 cells) (Table S2). The cellular uptake efficiency of **Ir-1–3** did not correlate well with their lipophilicities, probably because the overall outcome of cellular uptake is also influenced by other factors (e.g. molecular size).

The antiproliferative activity of complexes **Ir-1–3** against HeLa, human lung adenocarcinoma epithelial (A549), cisplatin-resistant A549 (A549R), human hepatocellular liver carcinoma (HepG2), and human normal liver (LO2) cells were evaluated by 3-(4,5-dimethylthiazol-2-yl)-2,5-diphenyltetrazolium bromide (MTT) assay, and cisplatin was also tested as a reference. As shown in Table 1, the viability of these cancer cell lines was significantly inhibited by **Ir-1–3**, with IC_{50} values ranging from 4.7 to 18.1 μM. Furthermore, they exhibited acceptable selectivity toward human cancer cells over non-cancerous cells, and the selectivity fold varied with the auxiliary ligands of iridium(III) complexes, indicating that the auxiliary ligands of iridium(III) complexes may affect the selectivity of iridium(III) complexes toward human cancer cells over non-cancerous cells. More importantly, **Ir-1–3** exhibited higher antiproliferative activity compared to cisplatin. Meanwhile, **Ir-1–3** also exhibited ~5- to 10-fold higher cytotoxic effect on A549R cells than cisplatin, indicating that these compounds have potential to overcome cisplatin resistance.

Inhibition of cell migration and colony formation

JMJD histone demethylase has been reported to play a role in promoting the metastasis of cancer cells.[25,55] Meanwhile, inhibition of cancer cell metastasis is a critical issue in tumor therapy.[56] Given the ability of **Ir-1–3** to inhibit JMJD activity and increase the expression of histone methylation in cells, the effects

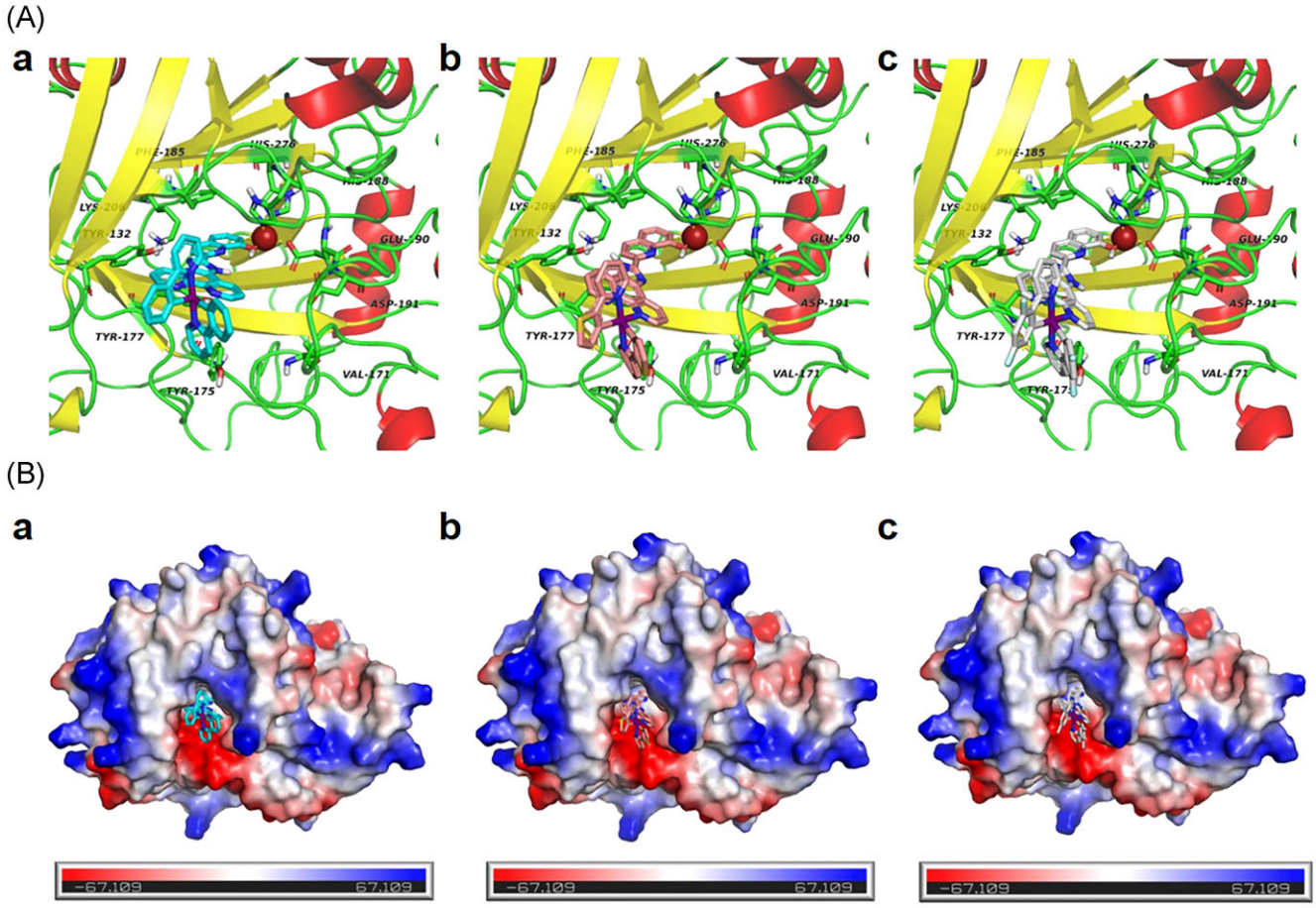

Fig. 2 Docking results of **Ir-1–3** with JMJD (PDB code: 5ANQ). (A) Docked conformations for **Ir-1** (a), **Ir-2** (b), and **Ir-3** (c) with JMJD. The red sphere represents the active center Fe^{2+} of JMJD. (B) Electrostatic surface diagrams of **Ir-1** (a), **Ir-2** (b), and **Ir-3** (c) are bound to JMJD. The blue color in the electrostatic surface represents the positive charge, the red color represents the negative charge, and the white color represents the region with very low or no charge, i.e. the non-polar region.

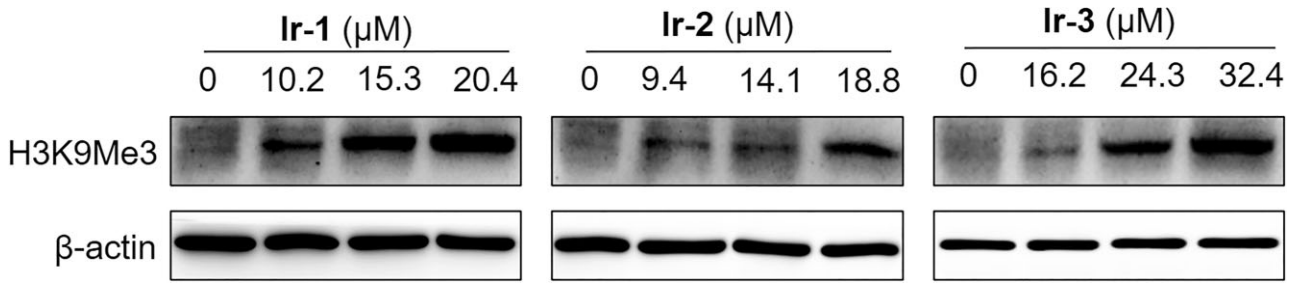

Fig. 3 Dose-dependent effects of **Ir-1–3** on H3K9Me3 after 24 h of treatment.

of the compounds on tumor cell migration were also evaluated. As shown in the wound healing assay (Fig. 4A), after treating HeLa cells with 2 × IC_{50} concentration of **Ir-1–3**, shorter migration distances were found at 24 and 36 h compared to vehicle-treated cells. And after incubation for 36 h, **Ir-1–3** could efficiently impede HeLa cells' migration at a wound closure ratio of 2.5–2.7%, which was much lower than that of the control group (17.8%) (Fig. 4B). In addition, colony formation is a key feature of malignant cancer cells,[57] thereby the inhibition of colony formation induced by **Ir-1–3** was assessed. As shown in Fig. 4C and D, the colony formation was effectively suppressed upon incubation with **Ir-1–3**. These results demonstrate that **Ir-1–3** can effectively inhibit cancer cell metastasis.

Cell cycle arrest

It has been reported that the JMJD inhibitors can inhibit cell proliferation via inducing cell cycle arrest.[58,59] Hence, the effects of **Ir-1–3** on cell cycle distribution were examined via flow cytometry with propidium iodide (PI) staining. As shown in Fig. 5 and Table S3, **Ir-1** could effectively arrest the cell cycle at the G2/M phase in a concentration-dependent manner, whereas **Ir-2** and **Ir-3** arrested the cell cycle at the G2/M phase only at higher

Table 1. IC_{50} values of the tested compounds against different cell lines[a]

Compounds	IC_{50} (μM)				
	HeLa	A549	A549R	HepG2	LO2
Ir-1	5.1 ± 0.5	12.9 ± 2.2	18.1 ± 1.9	11.5 ± 0.1	17.8 ± 0.4
Ir-2	4.7 ± 0.3	5.5 ± 1.1	8.9 ± 0.4	7.8 ± 0.4	6.9 ± 1.9
Ir-3	8.1 ± 1.4	10.0 ± 2.7	12.0 ± 1.9	10.2 ± 0.7	9.8 ± 1.6
Cisplatin	23.4 ± 0.7	21.5 ± 1.7	89.3 ± 3.1	21.5 ± 1.4	27.2 ± 0.8

[a]IC_{50} values are drug concentrations necessary for 50% inhibition of cell viability. The data are presented as mean ± standard deviation (SD) and cell viability is assessed after 48 h incubation.

concentrations. Quantitative cell cycle distribution data showed that cells were exposed to **Ir-1–3** at the highest tested concentration (4 × IC_{50}) for 24 h, and the percentage of cells in the G2/M phase increased from 16.7% (control) to 34.6% (**Ir-1**, 20.4 μM), 25.3% (**Ir-2**, 18.8 μM), and 46.7% (**Ir-3**, 32.4 μM), respectively.

Cellular localization and uptake mechanisms

The subcellular localization and cellular transport pathways of metal-based anticancer drugs can provide more hints on their antitumor mechanisms.[12,60] Herein, the subcellular localization and cellular transport pathways of **Ir-1–3** were monitored by tracking the luminescence of the complexes using confocal microscopy. As shown in Fig. 6A, **Ir-1–3** could be effectively taken up by HeLa cells and emitted intense dot-like luminescence in the cytoplasm after 2.5 h incubation at 37°C. Meanwhile, the phosphorescence signals of **Ir-1–3** inside the cells highly overlapped with the punctate structures of LysoTracker Deep Red FM (LTDR), and Pearson's colocalization coefficients were between 0.65 and 0.78. In contrast, the luminescent regions of **Ir-1–3** had little overlap with MitoTracker Deep Red FM (MTDR) (Fig. 6B). These results indicate that **Ir-1–3** mainly distribute in lysosomes instead of mitochondria.

We further examined the cellular uptake mechanisms of **Ir-1–3** by confocal microscope. Incubation of HeLa cells with **Ir-1–3** at low temperature (4°C) or pretreatment with metabolic inhibitor carbonyl cyanide m-chlorophenyl hydrazone (CCCP) resulted in a significant decrease in cellular uptake efficiency (Fig. S9). While, the cellular uptake levels of **Ir-1–3** were not affected in cells pretreated with chloroquine, which regulates endocytosis by inhibiting the acidification of endosomes. The results infer that **Ir-1–3** are transported into the cell membrane primarily via an energy-dependent mechanism instead of an endocytic pathway, which is similar to other cyclometalated Ir(III) complexes previously reported.[54,61]

Lysosomal damage

Metal complexes localized in lysosomes have been reported to induce lysosomal dysfunction, which is considered to be one of

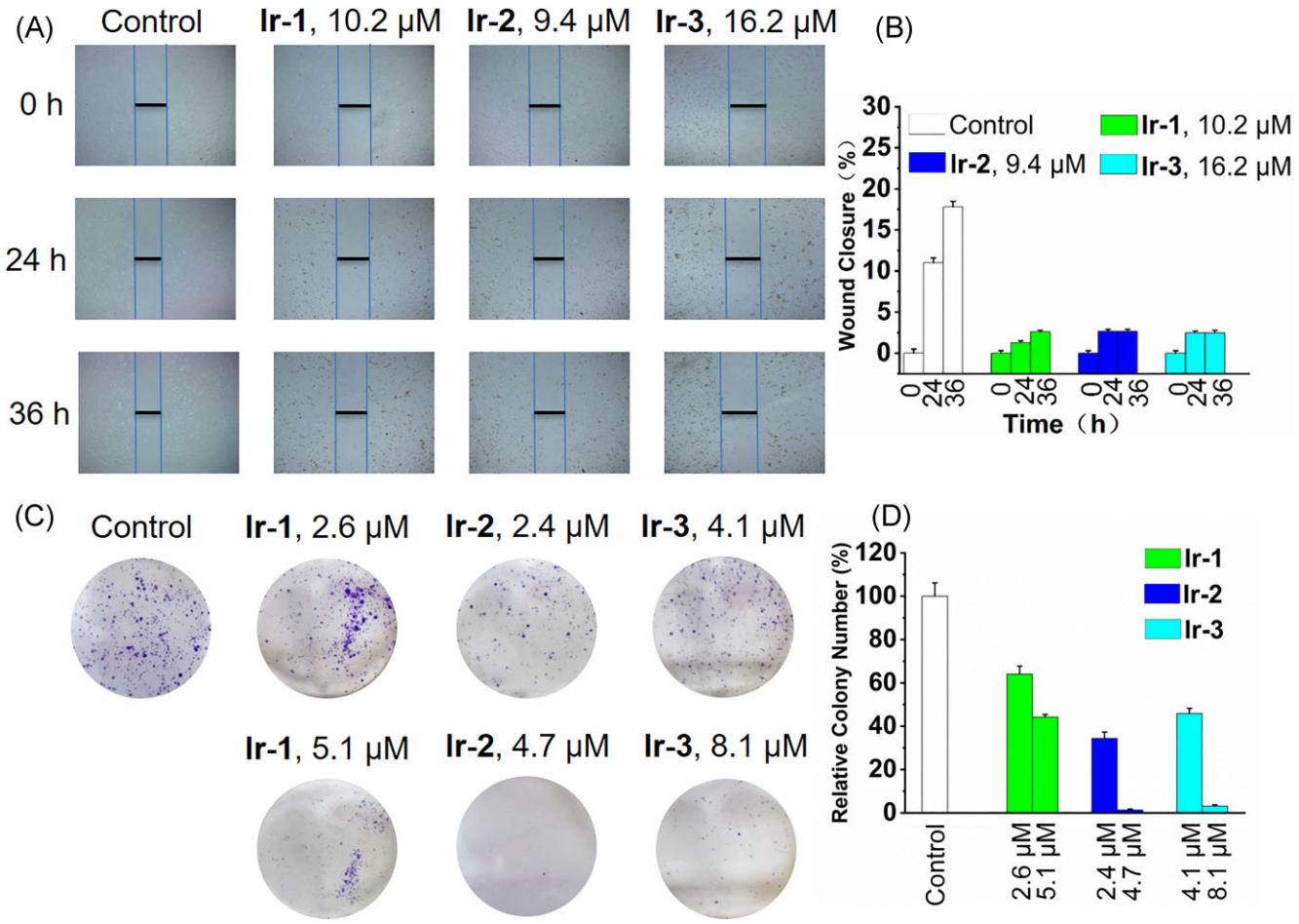

Fig. 4 (A) Representative pictures of a wound healing assay of HeLa cells after treated with **Ir-1–3** for 0 h, 24 h, and 36 h. The black lines indicate the distance of the wound. (B) Quantitative data of wound healing. Wound closure (%) = [1–(width at indicated time)/(width at 0 h)] × 100%. (C) Images of colony formation after treatment with **Ir-1–3**. (D) Quantitative data of colony formation assays.

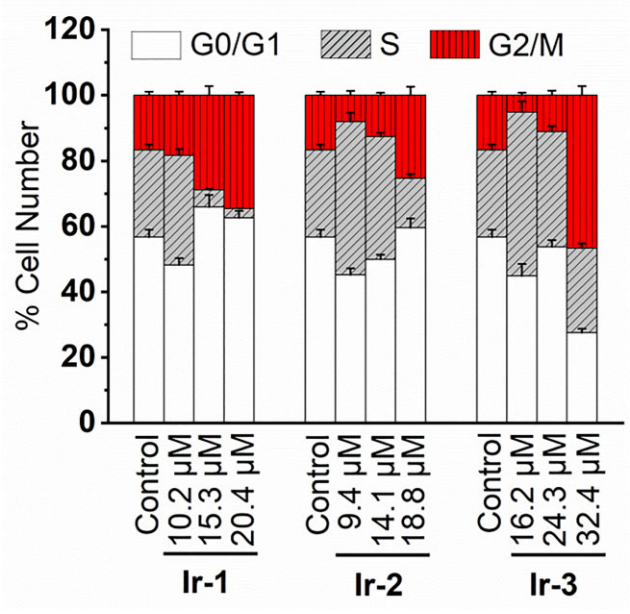

Fig. 5 Quantitative cell cycle distribution data for HeLa cells after treatment with **Ir-1–3** for 24 h.

the main toxicity paradigms of lysosome-targeted metal-based anticancer complexes.[38,62] Thus, the lysosomal integrity of HeLa cells after treatment with **Ir-1–3** was tested with acridine orange (AO) staining. AO is a common fluorescent indicator of acidic organelles and can be used to study the integrity of lysosomes because it emits red fluorescence in lysosomes and green fluorescence in cytosol and nuclei.[34] As shown in Fig. 7A, vehicle-treated cells displayed distinct red fluorescence in lysosomes. However, after HeLa cells were treated with **Ir-1–3** for 6 h, the red fluorescence in cells remarkably decreased in a concentration-dependent manner, implying that the lysosomes were seriously damaged. Additionally, upon treatment of HeLa cells with **Ir-1–3** at the much higher dose (40 μM) for 5 h, LTDR was diffusely distributed in cells and lost its ability to image lysosomes in cells, meaning the acidity in the lysosomal microenvironment is altered (Fig. S10). These results validate that **Ir-1–3** can increase the permeability of lysosomes, therefore disrupting the acidic environment of lysosomes.

LMP can evoke the release of lysosomal hydrolases, such as cathepsin B, from lysosomes to the cytosol to initiate apoptosis.[63] The effect of **Ir-1–3** on cathepsin B release was examined using the fluorogenic substrate Magic Red MR-$(RR)_2$.[64] As depicted in Fig. 7B, the red fluorescence of Magic Red MR-$(RR)_2$ was punctate in HeLa cells for the control cells, showing cathepsin B mostly aggregated in lysosomes. While, with the increase of concentration of **Ir-1–3**, the red fluorescence gradually showed a dispersive pattern in the cytoplasm, which indicated that **Ir-1–3** induced lysosomal damage and released cathepsin B from the lysosomes to the cytosol.

Apoptosis induction

Lysosomal damage and JMJD inhibition have been reported to be closely related to RCD.[17,62,65] Among them, apoptosis is the most common form of RCD. Cells undergoing apoptosis are associated with a series of defined morphological changes and biological events, such as cell shrinkage, plasma membrane blistering, nuclear fragmentation, apoptotic-body formation, accompanied by phosphatidylserine externalization, and caspases activation, etc.[66,67] To investigate whether **Ir-1–3** induced apoptosis in HeLa cells, the changes in nuclei morphology of **Ir-1–3**-treated HeLa cells were first observed by 2′-(4-ethoxyphenyl)-5-(4-methyl-1-piperazinyl)-2,5′-bi-1H-benzimidazole trihydrochloride (Hoechst 33342) staining. As shown in Fig. 8A, the nuclei of vehicle-treated cells showed a round and homogeneous staining pattern. While after treatment of HeLa cells with **Ir-1–3**, the proportion of nuclei with apoptotic morphology (nuclear fragmentation, chromatin condensation, and apoptotic-body formation)[68] increased progressively in a concentration-dependent manner.

Apoptosis induced by **Ir-1–3** was further verified quantitatively by flow cytometric analysis with Annexin V and PI double staining, with cisplatin as a control (Fig. 8B). The results showed that, compared with the control cells, cells exposed to **Ir-1–3** increased the percentage of apoptotic cells in a concentration-dependent manner. And the percentage of cells in the early and late

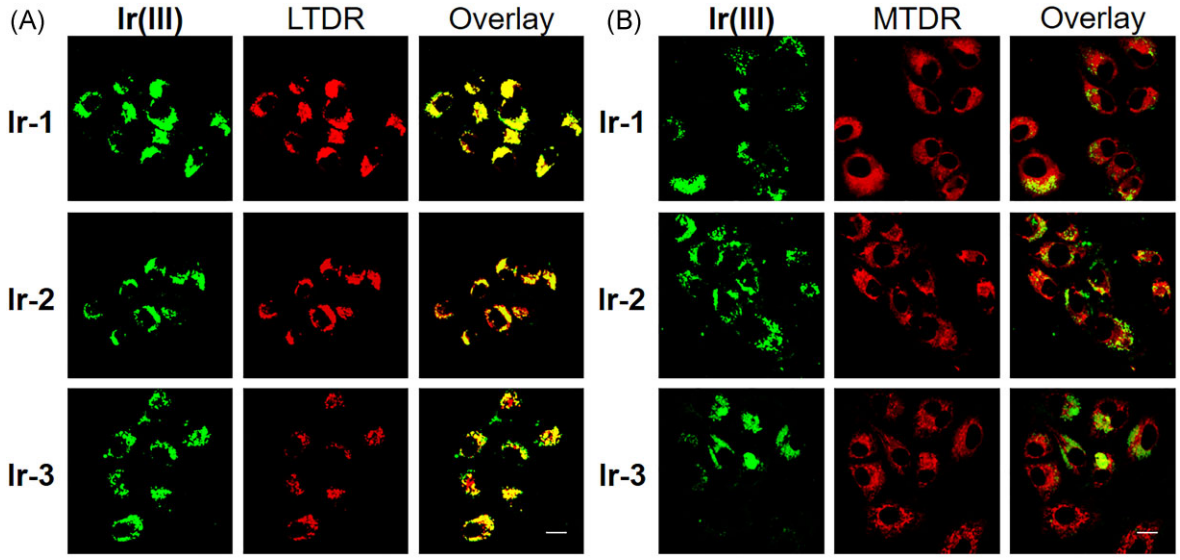

Fig. 6 The confocal microscopic images of HeLa cells co-labeled with **Ir-1–3** (20 μM, 2.5 h) and LTDR (50 nM, 0.5 h) (A) or MTDR (150 nM, 0.5 h) (B) [λ_{ex} = 402 nm (for **Ir-1–3**), 633 nm (for MTDR and LTDR); λ_{em} = 520 ± 20 nm (for **Ir-3**), 570 ± 20 nm (for **Ir-1** and **Ir-2**), and 665 ± 20 nm (for MTDR and LTDR)]. Scale bar: 20 μm.

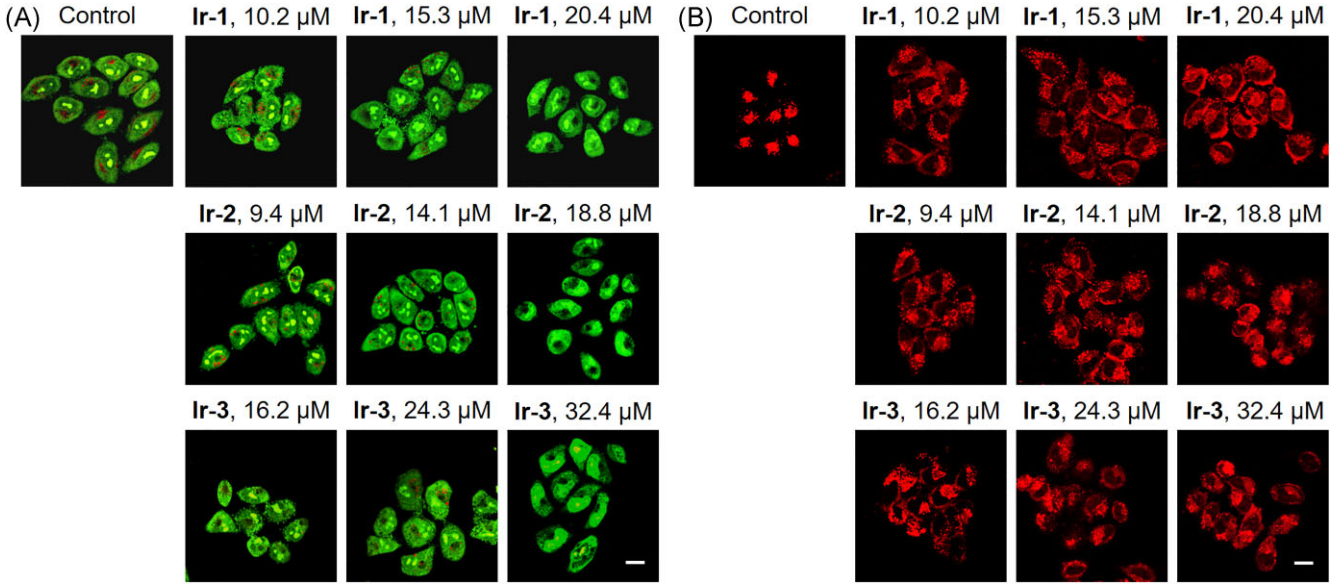

Fig. 7 (A) Detection of lysosomal disruption upon **Ir-1–3** treatment in HeLa cells by AO staining [λ_{ex} = 488 nm, λ_{em} = 510 ± 20 nm (green) and 625 ± 20 nm (red)]. (B) Observation of cathepsin B release from lysosomes to the cytosol upon **Ir-1–3** treatment in HeLa cells using Magic Red MR-$(RR)_2$ as a fluorogenic substrate (λ_{ex} = 543 nm, λ_{em} = 630 ± 20 nm). Scale bar: 20 μm.

apoptotic stages ranged from 7.42% (control) to 37.30% (**Ir-1**, 20.4 μM), 19.30% (**Ir-2**, 18.8 μM), and 58.30% (**Ir-3**, 32.4 μM), respectively.

The cleavage of Poly(ADP-ribose) polymerase (PARP), a substrate protein of caspase-3, has been identified as the biomarker of apoptosis.[69] As a member of the cysteine protease family, caspase-3 plays a crucial significant role in mediating apoptosis under various stimuli.[70] Therefore, the cleavage of caspase-3 and PARP were assessed by Western blot. As depicted in Fig. 8C, caspase-3 and PARP were cleaved in a dose-dependent manner after incubation with **Ir-1–3**. These results manifest that **Ir-1–3** induce apoptotic cell death through caspase-dependent mechanisms, which is also the main pathway for iridium(III) complexes-induced apoptosis.[71,72]

Mitochondrial dysfunction and cellular ROS production

LMP can cause the release of cathepsins, which trigger substrate degradation, disruption of mitochondrial integrity, and caspase-dependent cell death.[35] The influence of **Ir-1–3** on mitochondrial integrity was monitored by detecting the changes in red/green fluorescence intensity ratio of 5,5′,6,6′-tetrachloro-1,1′-3,3′-tetraethyl-benzimidazolylcarbocyanineiodide (JC-1).[73] In control cells, JC-1 mainly existed in the form of aggregates and emitted red fluorescence, suggesting the high MMP (Fig. 9A). But after treatment of HeLa with **Ir-1–3** for 12 h, a prominent decrease in MMP was observed, and the proportion of cells with depolarized mitochondria increased from 4.3% (control) to 42.6% (**Ir-1**, 20.4 μM), 57.6% (**Ir-2**, 18.8 μM), and 63.8% (**Ir-3**, 32.4 μM), respectively. The results manifest that **Ir-1–3** can cause mitochondrial dysfunction and eventually activate the mitochondrial apoptotic pathway.

Mitochondrial dysfunction and abnormal production of ROS are two closely related events involved in cancer cell death caused by many anticancer agents.[10,74] Intracellular ROS levels were investigated by confocal microscopy using 2′,7′-dichlorofluorescein diacetate (H_2DCFDA) as the fluorescent probe. H_2DCFDA is a non-fluorescent cell-permeable dye, but can turn into highly fluorescent 2′,7′-dichlorofluorescein (DCF) by the oxidation of intracellular ROS.[75] As depicted in Fig. 9B, compared to vehicle-treated cells, a concentration-dependent increase in ROS levels was observed in HeLa cells treated with **Ir-1–3**. Flow cytometric analysis (Fig. S11) also showed that, compared with the control cells, the DCF mean fluorescence intensity of cells treated with **Ir-1–3** at 4 × IC_{50} increased by 2.1-, 2.4-, and 3.0-fold, respectively. Furthermore, N-acetyl-L-cysteine (NAC), a ROS scavenger, could lead to marked inhibition of cell death induced by **Ir-1–3** (Fig. S12). These results demonstrate that ROS plays an important role in **Ir-1–3**-induced cell death.

Autophagy induction

Autophagy is a lysosomal degradation pathway through lysosomal hydrolases that allows the degradation of damaged or unnecessary cytoplasmic contents, including dysfunctional proteins and organelles.[76] Autophagy plays an important role in cellular homeostasis, cancer prevention, and treatment.[77] Besides, lysosome-targeted metal-based compounds have been reported to induce both apoptosis and autophagy in cancer cells.[46,48,78] Therefore, we tested whether **Ir-1–3** could induce autophagy by Western blot analysis. During autophagy, LC3-I will be converted into LC3-II, which has been identified as an autophagy marker.[79] When cells undergo autophagy and lysosomal functions are intact, LC3-II levels are elevated while p62 levels are reduced. However, when autophagy is blocked due to impaired lysosomal functions, LC3-II and P62 levels are increased.[49,80] As depicted in Fig. S13, the ratio of LC3-II to LC3-I increased significantly after treatment with **Ir-1**, **Ir-2**, and rapamycin compared to the control. Meanwhile, the ratio of LC3 (LC3-II/LC3-I) conversion induced by **Ir-1** and **Ir-2** showed a marked concentration-dependent behavior (Fig. 10). In addition, **Ir-1–3** could also activate p62, which signified that autophagy induced by **Ir-1–3** was blocked owing to the damaged lysosomes.

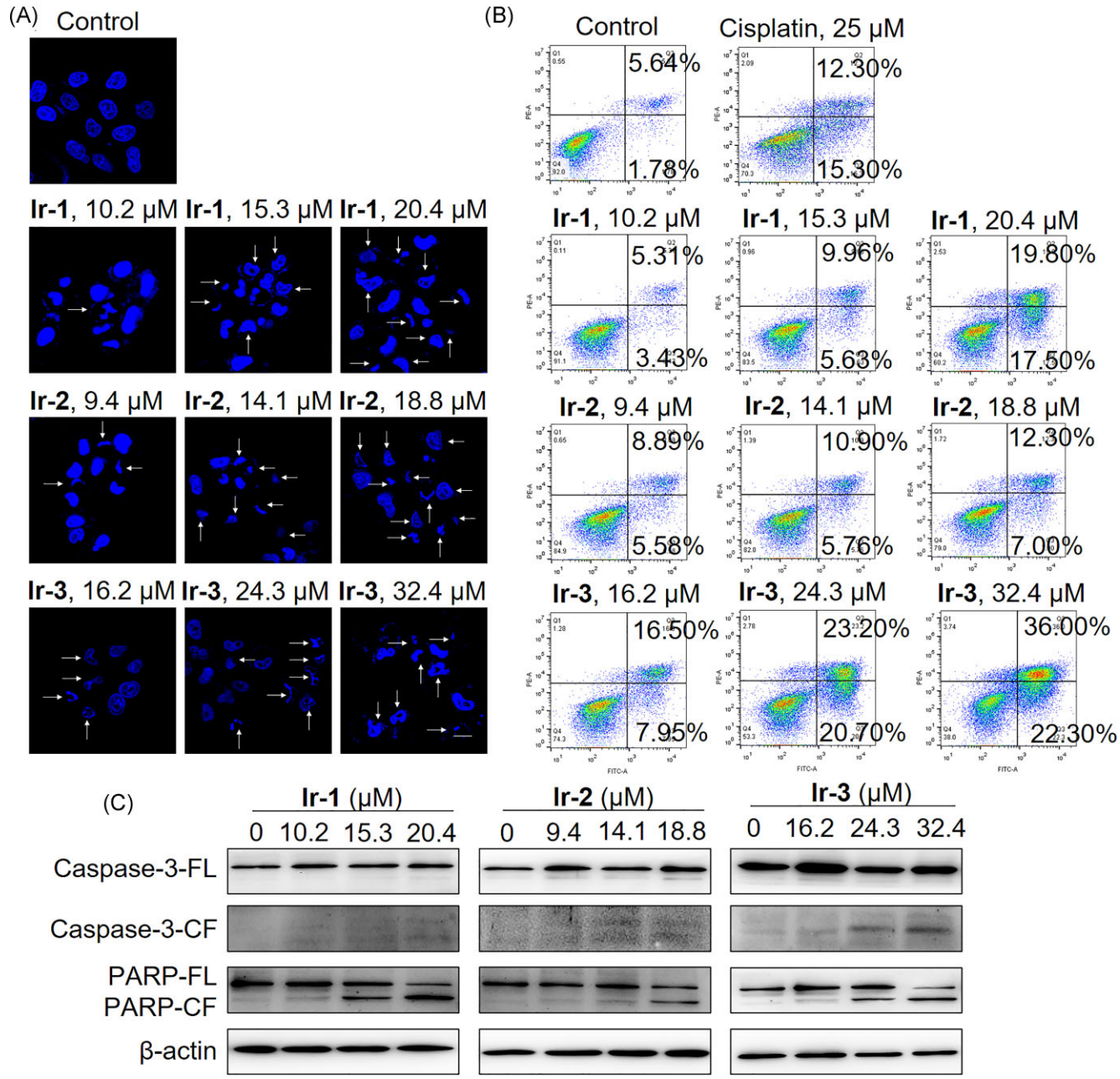

Fig. 8 (A) Hoechst 33 342 staining for the nuclei (λ_{ex} = 405 nm, λ_{em} = 460 ± 20 nm). Scale bar: 20 μm. The arrows indicate the apoptotic morphological nuclei. (B) Flow-cytometric quantification of Annexin V-FITC/PI labeled cells after treatment with **Ir-1–3** for 24 h [λ_{ex} = 488 nm, λ_{em} = 530 ± 20 nm (for annexin V) and 620 ± 20 nm (for PI)]. (C) Western blot analysis of the apoptosis-related protein (caspase-3, PARP) in cells after incubation with **Ir-1–3** for 24 h (FL, full length; CF, cleaved form).

In vivo antitumor activity

To test whether iridium complexes could inhibit tumor growth *in vivo*, we assessed the biological efficacy of **Ir-1** in an H22 mouse model. As shown in Fig. 11A and C, after intratumoral injection of 5 mg/kg **Ir-1** into H22-bearing mice, the tumor volume was much less than those of the solvent control group. After 15 days, the tumor volume of **Ir-1**-treated mice decreased by ~57% compared with the solvent control group. Importantly, no significant difference was found in body weight among the solvent control group and the drug administration group (Fig. 11B), suggesting that **Ir-1** has no severe side effects in these conditions. Having seen that iridium complexes could increase the expression of histone methylation levels *in vitro*, we next assessed whether **Ir-1** could also alter the expression of histone methylation levels *in vivo*. Therefore, the expression of H3K9Me3 in tumor tissues was detected by Western blot. As shown in Fig. 11D, **Ir-1** could increase the expression of H3K9Me3, indicating the inhibition of JMJD activity.

Experimental section

Materials and instruments

$IrCl_3 \cdot nH_2O$, ppy, thpy, dfppy, NAC, NH_4PF_6, chloroquine, CCCP, and 5,6-diamino-1,10-phenanthroline were obtained from Alfa Aesar. 8-hydroxy-2-quinolinecarboxaldehyde was purchased from Innochem. Cisplatin, MTT, DMSO, AO, H_2DCFDA, and

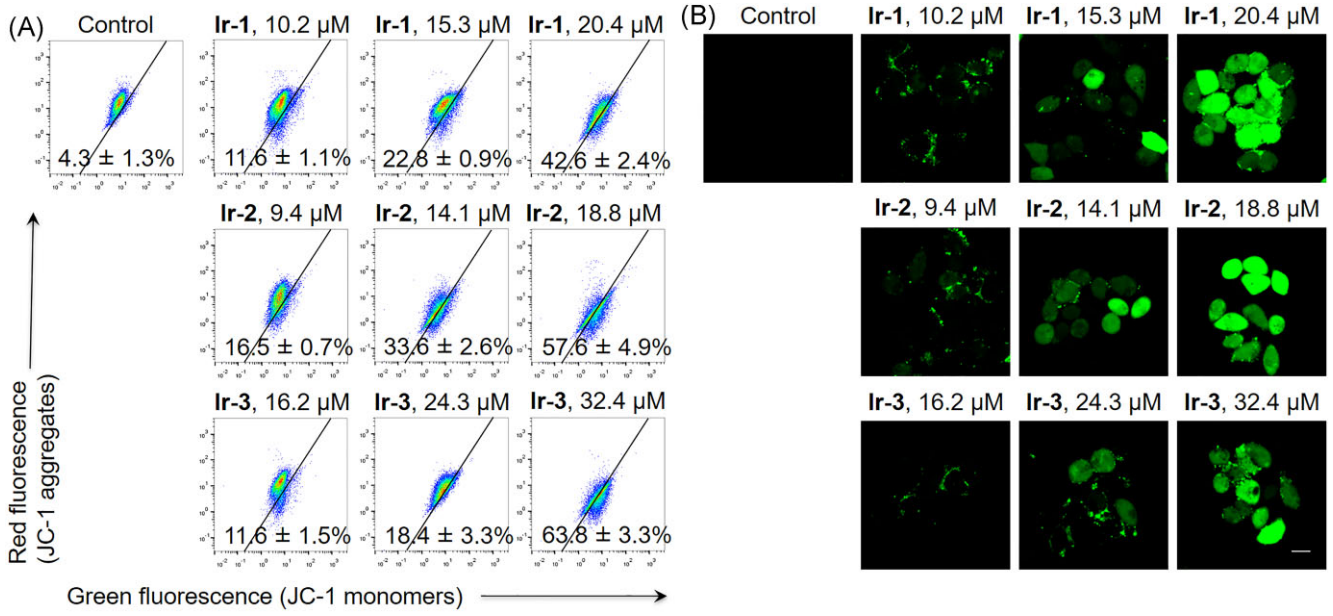

Fig. 9 (A) The loss of MMP examined by flow cytometry with JC-1 staining after treatment with **Ir-1–3** for 12 h [λ_{ex} = 488 nm, λ_{em} = 530 ± 20 nm for JC-1 monomer (green) and 585 ± 20 nm for JC-1 aggregates (red)]. (B) The intracellular ROS levels were examined by confocal microscopy with H_2DCFDA staining after treatment with **Ir-1–3** for 6 h (λ_{ex} = 488 nm, λ_{em} = 530 ± 20 nm). Scale bar: 20 μm.

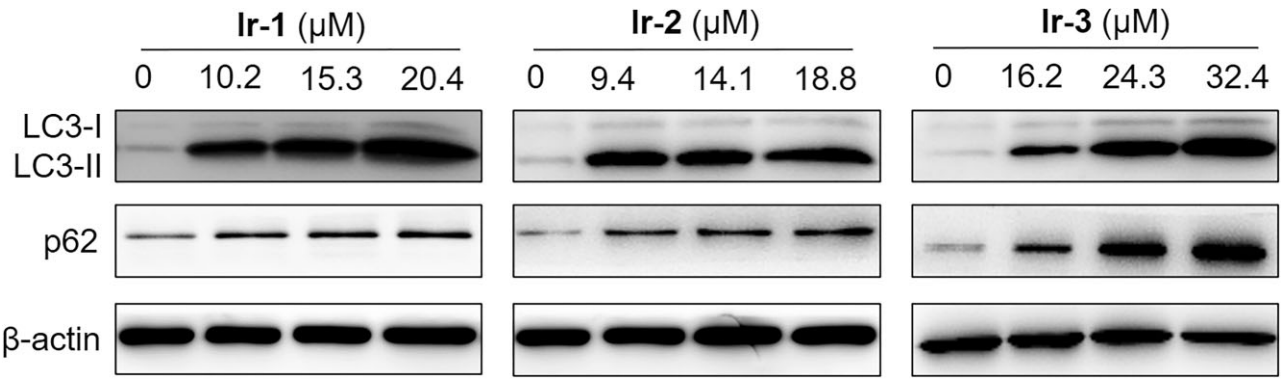

Fig. 10 Western blot analysis of autophagy-related protein (LC3, p62) in HeLa cells treated with **Ir-1–3** for 24 h.

Hoechst 33342 were obtained from Sigma Aldrich. Cell Cycle and Apoptosis Analysis Kit, Annexin V-FITC Apoptosis Detection Kit, PBS, crystal violet, 4% paraformaldehyde, and JC-1 were purchased from Beyotime Biotechnology. MTDR and LTDR were purchased from Life Technologies. Magic Red MR-$(RR)_2$ was purchased from Immunochemistry Tech. Dulbecco's modified Eagle medium (DMEM), Fetal bovine serum, and penicillin-streptomycin were obtained from Gibco. Primary antibodies against H3K9Me3, caspase-3, PARP, p62, and LC-3 were obtained from Cell Signaling Technology. Male BALB/c mice were purchased from Beijing Weitong Lihua Experimental Animal Center.

NMR spectra were recorded on a Bruker Avance 600 spectrometer. ESI-MS spectra were carried out using an LCQ DECA XP spectrometer. Cell viability measurements were carried out using a SpetraMax M2 plate reader. Cell imaging images were conducted on a Nikon A1R/A1 laser-scanning confocal microscope, and flow cytometric analyses were conducted on a CyFlow Space flow cytometer.

Preparation of iridium(III) complexes

Three Ir(III) chloro-bridged dimers $[Ir(ppy)_2Cl]_2$,[81] $[Ir(thpy)_2Cl]_2$,[82] $[Ir(dfppy)_2Cl]_2$[83] and the intermediate compounds $[Ir(C^N)_2$(5,6-diamino-1,10-phenanthroline)$](PF_6)$[50] were synthesized following the literature methods. The synthetic routes of **Ir-1–3** were illustrated in Scheme S1. And **Ir-1–3** were converted into hexafluorophosphate by ammonium hexafluorophosphate for the biological test.

Synthesis of **Ir-1**: $[Ir(ppy)_2$(5,6-diamino-1,10-phenanthroline)$](PF_6)$ (0.1 g, 0.117 mmol) and 8-hydroxy-2-quinolinecarboxaldehyde (0.024 g, 0.117 mmol) was refluxed in methanol for 24 h at 65°C in the dark. Upon completion, the above solvent was added to excess saturated NH_4PF_6 aqueous solution and stirred for another 6 h. The solvent was then removed by a rotary evaporator. The crude solid was purified using column chromatography on silica gel by elution with CH_2Cl_2/CH_3OH (30:1, v/v). Yield: 0.094 g (orange powder), 80%. ^{1}H NMR (600 MHz, [D_6] DMSO) δ 9.84 (s, 1H), 9.15 (d, J = 31.4 Hz, 2H), 8.57 (d, J = 8.5 Hz, 1H), 8.48 (d, J = 8.5 Hz, 1H), 8.31 (d, J = 8.1 Hz, 2H), 8.26–8.09

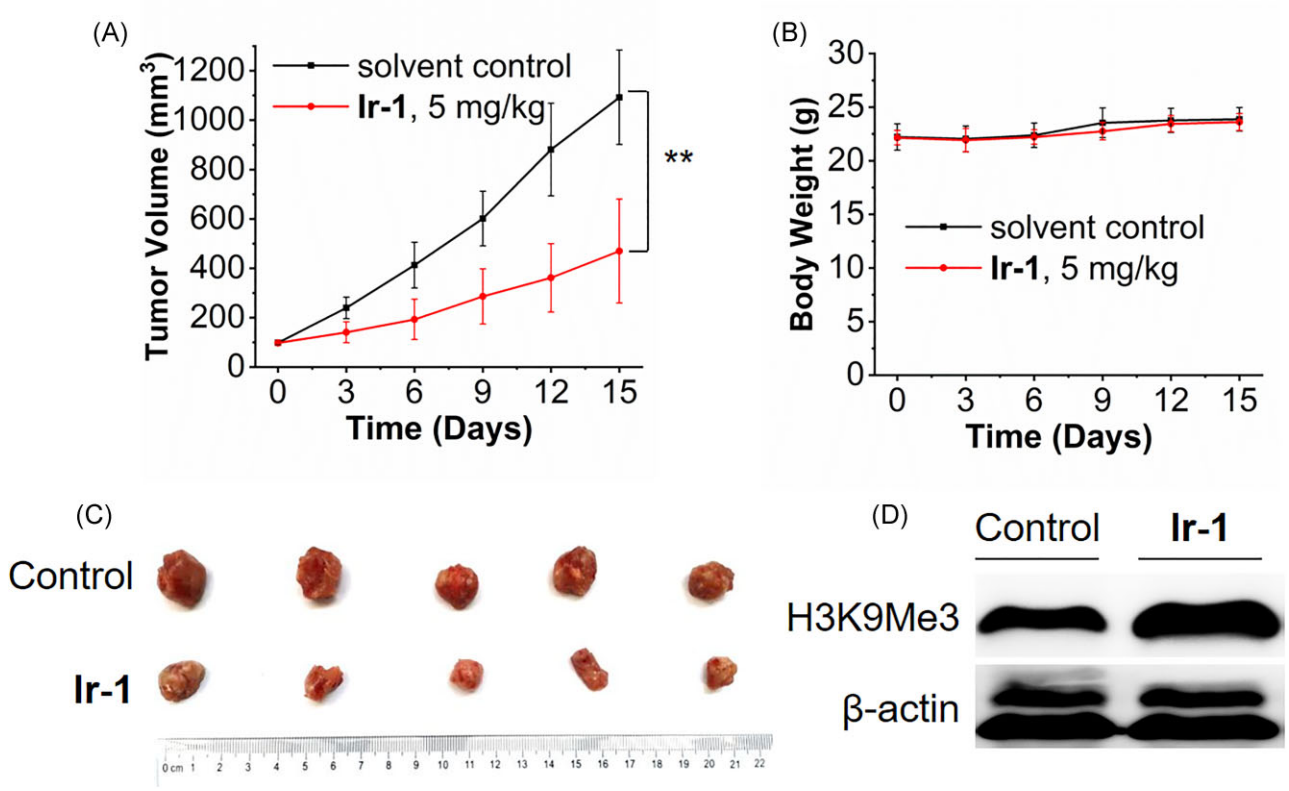

Fig. 11 Antitumor activity of **Ir-1** in H22 xenograft-bearing mice. The average tumor volume (A) and body weight (B) of BALB/c mice in solvent control and **Ir-1** (5 mg/kg) groups ($n = 5$) (** $P < 0.01$). (C) Photographs of tumors removed from mice. (D) Western blot of H3K9Me3 expression in tumor tissues.

(m, 4H), 8.00 (d, $J = 7.7$ Hz, 2H), 7.91 (t, $J = 7.5$ Hz, 2H), 7.65–7.40 (m, 4H), 7.18 (d, $J = 4.0$ Hz, 1H), 7.11–6.96 (m, 6H), 6.32 (d, $J = 7.2$ Hz, 2H). ESI-MS (CH_3OH): m/z 432.6064 $[M\text{-}PF_6 + H]^{2+}$, 864.2040 $[M\text{-}PF_6]^+$. Anal. Calcd for $C_{44}H_{29}F_6IrN_7OP$ (%): C, 52.38; H, 2.90; N, 9.72; found: C, 52.18; H, 3.01; N, 9.59.

Synthesis of **Ir-2**: The compound **Ir-2** was synthesized by a similar method to **Ir-1** except that $[Ir(ppy)_2(5,6\text{-diamino-}1,10\text{-phenanthroline})](PF_6)$ was replaced by $[Ir(thpy)_2(5,6\text{-diamino-}1,10\text{-phenanthroline})](PF_6)$. Yield: 0.096 g (reddish brown powder), 82%. ^{1}H NMR (600 MHz, [D_6] DMSO) δ 9.79 (s, 1H), 9.12 (d, $J = 38.0$ Hz, 2H), 8.53 (d, $J = 8.5$ Hz, 1H), 8.44 (d, $J = 8.4$ Hz, 1H), 8.17 (d, $J = 28.2$ Hz, 4H), 7.81–7.76 (m, 4H), 7.73 (d, $J = 4.6$ Hz, 2H), 7.49 (s, 2H), 7.41 (s, 2H), 7.13 (s, 1H), 6.85 (t, $J = 5.2$ Hz, 2H), 6.30 (d, $J = 4.3$ Hz, 2H). ESI-MS (CH_3OH): m/z 438.5591 $[M\text{-}PF_6 + H]^{2+}$, 876.1091 $[M\text{-}PF_6]^+$. Anal. Calcd for $C_{40}H_{25}F_6IrN_7OPS_2$ (%): C, 47.06; H, 2.47; N, 9.60; found: C, 47.38; H, 2.27; N, 9.43.

Synthesis of **Ir-3**: The compound **Ir-3** was synthesized by a similar method to **Ir-1** except that $[Ir(ppy)_2(5,6\text{-diamino-}1,10\text{-phenanthroline})](PF_6)$ was replaced by $[Ir(dfppy)_2(5,6\text{-diamino-}1,10\text{-phenanthroline})](PF_6)$. Yield: 0.091 g (yellow powder), 78%. ^{1}H NMR (600 MHz, [D_6] DMSO) δ 9.88 (s, 1H), 9.24 (d, $J = 26.7$ Hz, 2H), 8.60 (d, $J = 8.6$ Hz, 1H), 8.52 (d, $J = 8.5$ Hz, 1H), 8.33 (d, $J = 9.0$ Hz, 4H), 8.17 (d, $J = 33.7$ Hz, 2H), 8.01 (t, $J = 7.6$ Hz, 2H), 7.64 (d, $J = 10.1$ Hz, 2H), 7.54 (d, $J = 7.2$ Hz, 2H), 7.23 (d, $J = 6.4$ Hz, 1H), 7.12 (t, $J = 6.7$ Hz, 2H), 7.09–7.03 (m, 2H), 5.74 (d, $J = 7.3$ Hz, 2H). ESI-MS (CH_3OH): m/z 468.5877 $[M\text{-}PF_6 + H]^{2+}$, 936.1667 $[M\text{-}PF_6]^+$. Anal. Calcd for $C_{44}H_{25}F_{10}IrN_7OP$ (%): C, 48.89; H, 2.33; N, 9.07; found: C, 49.12; H, 2.09; N, 8.86.

Binding of Ir-1–3 with iron ions

The solution (2×10^{-5} M) of **Ir-1–3** in H_2O/DMSO (1:1, v/v) was prepared, and then the aqueous solutions of $FeCl_2$ and $FeCl_3$ were continuously added, and the changes in UV/Vis absorption spectra were measured. The excitation wavelength of **Ir-1–3** was 405 nm.

Molecular docking

Dockings of **Ir-1–3** and JMJD were carried out by AutoDock 4.2, using the Lamarckian genetic algorithm method.[84] The crystal structure of JMJD (PDB ID: 5ANQ) was retrieved from the protein data bank (PDB). A docking box of 60 × 60 × 60 points with a grid spacing of 0.375 Å was used in each calculation. The center of the box was set as the metal ion in active site. The number of genetic algorithm calculations was set as 1000. All other parameters were used as default settings. For each of the docking cases, the conformation with the lowest energy was selected as the binding mode for analysis according to the Autodock scoring function. The output from AutoDock was rendered with the PyMOL program.

Western blot analysis

HeLa cells cultured in 100 mm cell culture dishes were exposed to different concentrations of **Ir-1–3** for 24 h. Cells were collected, washed twice with pre-cooled PBS, and lysed with RIPA buffer. The protein concentration was quantified using the BCA assay kit. Equal amounts of cellular total proteins were separated on sodium dodecyl sulfate-polyacrylamide gel electrophoresis (SDS-PAGE) and then transferred to the polyvinylidene difluoride membrane. After blocking, the membranes were incubated with primary antibodies against H3K9Me3, caspase-3, PARP, LC-3, and p62 at 4°C overnight and then incubated with secondary antibodies.

Lipophilicity

The lipophilicity of **Ir-1–3** was determined according to a previous procedure[85] and presented as log $P_{o/w}$ values. Log $P_{o/w}$ is defined as the logarithmic ratio of the concentration of **Ir-1–3** in n-octanol to that in the aqueous phase.

ICP-MS measurement

HeLa cells were seeded in 100 mm dishes and cultured overnight. The medium was replaced with a fresh medium containing **Ir-1–3** (20 μM). After 2.5 h incubation, the treated cells were washed with PBS, trypsinized, and collected. The cells were counted and digested with 60% HNO_3 for over 24 h. Intracellular iridium content was measured using the ELAN DRC II ICP-MS (USA).

In vitro cytotoxicity assay

The cytotoxicity of complexes **Ir-1–3** against HeLa, A549, A549R, HepG2, and LO2 cell lines was evaluated by MTT assay, and cisplatin was included as a control. Briefly, exponentially grown cells were seeded in 96-well plates and allowed to attach for 24 h. Cells were treated with a series of concentrations of the tested compounds for 44 h. Then, 20 μl MTT (5 mg/ml) was added to each well and incubated for another 4 h. The medium was removed, and the formazan products were dissolved in DMSO (150 μl/well) and shaken for 10 min. The cell viability was measured at 595 nm using a SpetraMax M2 plate reader.

Wound healing assay

Exponentially grown HeLa cells were seeded in 12-well plates. After the cells reached ~80–90% confluence, the cross lines on the center of each well were carefully made by a 200 μl sterile pipette tip. The scratched cells were washed away by PBS. Then, the cells were cultured in a serum-free culture medium containing the indicated concentrations of **Ir-1–3**. The wound closure was monitored and photographed by an inverted microscope at 0, 24, and 36 h.

Colony forming assay

HeLa cells were placed at a density of 600 cells per well in six-well plates. After 24 h, the medium was removed and replaced with a fresh medium containing the indicated concentrations of **Ir-1–3** for another 24 h. Then, the medium containing the tested complexes was removed again, and the cells were maintained in the fresh medium for 1 week. Cell colonies were fixed with 4% paraformaldehyde for 15 min and stained with 0.005% crystal violet for 30 min. The images of colonies were recorded with a digital camera.

Cell cycle analysis

HeLa cells seeded in six-well plates were treated with **Ir-1–3** for 24 h. The cells were harvested and fixed with 1 ml pre-cooled 70% aqueous ethanol. After storage at 4°C for 24 h, the cells were centrifuged at 800 g for 15 min and washed twice with pre-cooled PBS. DNA staining was achieved by re-suspending the immobilized cells in PBS containing PI (50 μg/ml) and RNAse (100 μg/ml) and then examined using flow cytometry.

Intracellular localization assay

HeLa cells were incubated with **Ir-1–3** (20 μM) at 37°C for 2.5 h and further co-incubated with the commercial mitochondrial probe MTDR (150 nM) or lysosomal probe LTDR (50 nM) for another 0.5 h. Cells were rinsed three times with PBS and visualized by confocal microscopy immediately. The excitation wavelengths of **Ir-1–3** and LTDR/MTDR were 405 nm and 633 nm, respectively. The emission was collected at 520 ± 20 nm for **Ir-3**, 570 ± 20 nm for **Ir-1** and **Ir-2**, and 665 ± 20 nm for LTDR and MTDR.

Cellular uptake mechanism studies

HeLa cells were incubated with the Ir(III) under different conditions, such as different temperatures and pretreatment with metabolic inhibitors or endocytic inhibitors. To investigate the effect of temperature on cellular uptake, HeLa cells were treated with **Ir-1–3** (20 μM) for 2.5 h at 4°C or 37°C. For inhibitors, HeLa cells were pretreated with CCCP (30 μM) or chloroquine (50 μM) for 1 h at 37°C, then exposed to **Ir-1–3** (20 μM) for 2.5 h at 37°C. After incubation, the cells were washed three times with PBS and visualized by confocal microscopy.

AO staining

After HeLa cells were seeded in confocal dishes and cultured overnight, the indicated concentrations of **Ir-1–3** were added and incubated for 6 h. The cells of each dish were washed with PBS and incubated with AO (5 μM) for 15 min. After incubation, the cells were washed again with PBS to remove the excess probe and visualized by confocal microscopy. Emission was collected at 510 ± 20 nm (green) and 625 ± 20 nm (red) upon excitation at 488 nm.

Detection of cathepsin B release

Cathepsin B activity was monitored using the fluorogenic substrate Magic Red MR-$(RR)_2$ according to the manufacturer's instructions. Briefly, HeLa cells were seeded in confocal dishes and cultured overnight, then treated with the indicated concentrations of **Ir-1–3** for 8 h. Upon completion, the fluorogenic substrate Magic Red MR-$(RR)_2$ was added and cultured for another 1 h. The media was removed, and the cells were rinsed twice with PBS before confocal imaging (λ_{ex} = 543 nm, λ_{em} = 630 ± 20 nm).

Hoechst 33 342 staining assay

HeLa cells were seeded in confocal dishes and cultured overnight. After treated with different concentrations of **Ir-1–3** for 24 h, the cells were washed twice with PBS carefully before fixed with 4% paraformaldehyde, and then stained with Hoechst 33342 (5 μg/ml). Eventually, the morphology of the cell nuclei was visualized by a confocal microscope (λ_{ex} = 405 nm, λ_{em} = 460 ± 20 nm).

Annexin V/PI staining

Analysis was performed according to the manufacturer's instructions. HeLa cells were seeded in six-well plates and cultured overnight. After treated with the indicated concentrations of **Ir-1–3** for 24 h, cells were harvested, re-suspended in 195 μl Annexin-binding buffer, then labeled with 5 μl Annexin V and 10 μl PI for 15 min in the dark. Subsequently, the samples were analyzed by flow cytometry [λ_{ex} = 488 nm, λ_{em} = 530 ± 20 nm (for annexin V) and 620 ± 20 nm (for PI)].

MMP assessment

HeLa cells were seeded in six-well plates in a humidified atmosphere and allowed to adhere overnight. The cells were treated with the concentrations of 2 × IC_{50}, 3 × IC_{50}, and 4 × IC_{50} of **Ir-1–3** for 12 h. After incubation, cells were harvested and stained

with JC-1 (5 μg/ml) in the dark for 20 min, followed by washing with a blank buffer. The cells were centrifuged for flow cytometric testing. The excitation was at 488 nm, and the dual emission was collected at 530 ± 20 nm for JC-1 monomer (green) and 585 ± 20 nm for JC-1 aggregates (red).

Measurement of intracellular ROS

HeLa cells were seeded in confocal dishes and cultured overnight. After treated with **Ir-1–3** at the indicated concentrations for 6 h, the cells were incubated with H_2DCFDA (10 μM) for 20 min at 37°C in the dark. Then, the cells were washed twice with serum-free DMEM to remove the excess probe. The fluorescence intensity of DCF in cells was immediately detected by confocal microscopy ($\lambda_{ex} = 488$ nm, $\lambda_{em} = 530 \pm 20$ nm).

Evaluation of antitumor activities *in vivo*

Male BALB/c mice aged 4–5 weeks were bred in compliance with the guidelines of the Institutional Animal Care and Use Committee of the Kunming University of Science and Technology. All studies involving animals were approved by the Animal Ethics Committee of Kunming University of Science and Technology. H22 cells (2×10^6) were suspended in 100 μl PBS, and the xenografts were established by subcutaneous injection. When the tumor reached ~80–120 mm^3, the mice were randomly assigned to two groups ($n = 5$) before the experiment. For the solvent control group, each mouse was injected with 100 μl PET diluent [6% poly(ethylene glycol) 400, 3% ethanol, 1% Tween 80, and 90% PBS]. For the experimental groups, mice were injected intratumorally with **Ir-1** (5 mg/kg, dissolved in 100 µl PET) every 3 days. Besides, tumor size and body weight of mice were also recorded every 3 days. After 15 days of treatment, the mice were sacrificed, and the tumors were separated. The calculation formula of tumor volume (V) was as follows: $V = ab^2 \times 0.5$, where a and b were the longest and shortest diameters of the tumor, respectively.

Statistical analysis

All biological experiments were performed at least twice with triplicates in each experiment. The quantitative data were presented as means ± SD.

Conclusions

In this work, we designed and synthesized three cyclometalated iridium(III) complexes, **Ir-1–3,** utilizing 8-hydroxyquinoline derivative as N^N ligands. The complexes can sequestrate the cofactor Fe^{2+} of JMJD histone demethylase and further inhibit its demethylation activity *in vitro*, and molecular docking studies also confirm **Ir-1–3** can interact with the active pocket of JMJD protein. Besides, **Ir-1–3** can block the cell cycle at the G2/M phase and inhibit cell migration and colony formation, which are associated with the inhibition of JMJD. And **Ir-1–3** are effectively taken up by HeLa cells via an energy-dependent mechanism and target to lysosomes. Further mechanisms indicate that **Ir-1–3** initiate caspase-dependent apoptosis through lysosomal damage, mitochondrial damage, and ROS elevation. Moreover, **Ir-1–3** can also induce autophagy. Promising antitumor efficacy with no severe side effects of **Ir-1** *in vivo* is also found, and the JMJD activity in tumor tissues is inhibited as well as *in vitro*. These results suggest that **Ir-1–3** are potential drug candidates with multifunctional antitumor effects for future antitumor therapy, which can inhibit JMJD and induce apoptosis and autophagy in cancer cells.

Supplementary material

Supplementary data are available at *Metallomics* online.

Acknowledgements

This work was supported by the National Natural Science Foundation of China (21967014, 22007042), Applied Basic Research Projects of Yunnan Province (202001AT070036), the Innovative Team of Yunnan Province (2019HC018), and High-level Scientific Research Foundation for Talent Introduction of Kunming University of Science and Technology (KKKP201826008).

Conflicts of interest

The authors declare no competing financial interests.

Data availability statements

The data underlying this article are available in the article and in its online supplementary material.

References

1. L. Kelland, The resurgence of platinum-based cancer chemotherapy, *Nat. Rev. Cancer*, 2007, 7 (8), 573–584.
2. S. Medici, M. Peana, V. M. Nurchi, J. I. Lachowicz, G. Crisponi and M. A. Zoroddu, Noble metals in medicine: latest advances, *Coord. Chem. Rev.*, 2015, 284 (1), 329–350.
3. J. Karges, M. Tharaud and G. Gasser, Polymeric encapsulation of a Ru(II)-based photosensitizer for folate-targeted photodynamic therapy of drug resistant cancers, *J. Med. Chem.*, 2021, 64 (8), 4612–4622.
4. K. C. Tong, C. N. Lok, P. K. Wan, D. Hu, Y. M. E. Fung, X. Y. Chang, S. Huang, H. Jiang and C. M. Che, An anticancer gold(III)-activated porphyrin scaffold that covalently modifies protein cysteine thiols, *Proc. Natl. Acad. Sci. U.S.A.*, 2020, 117 (3), 1321–1329.
5. W. Y. Zhang, S. Banerjee, G. M. Hughes, H. E. Bridgewater, J. I. Song, B. G. Breeze, G. J. Clarkson, J. P. C. Coverdale, C. Sanchez-Cano, F. Ponte, E. Sicilia and P. J. Sadler, Ligand-centred redox activation of inert organoiridium anticancer catalysts, *Chem. Sci.*, 2020, 11 (21), 5466–5480.
6. S. Kuang, F. Wei, J. Karges, L. Ke, K. Xiong, X. Liao, G. Gasser, L. Ji and H. Chao, Photodecaging of a mitochondria-localized iridium(III) endoperoxide complex for two-photon photoactivated therapy under hypoxia, *J. Am. Chem. Soc.*, 2022, 144 (9), 4091–4101.
7. L. Zhang, Y. Li, W. Che, D. Zhu, G. Li, Z. Xie, N. Song, S. Liu, B. Z. Tang, X. Liu, Z. Su and M. R. Bryce, AIE multinuclear Ir(III) complexes for biocompatible organic nanoparticles with highly enhanced photodynamic performance, *Adv. Sci.*, 2019, 6 (5), 1802050.
8. P. Zhang, H. Huang, S. Banerjee, G. J. Clarkson, C. Ge, C. Imberti and P. J. Sadler, Nucleus-targeted organoiridium-albumin conjugate for photodynamic cancer therapy, *Angew. Chem. Int. Ed.*, 2019, 58 (8), 2350–2354.
9. J. H. Zhu, G. X. Xu, J. Shum, L. C. Lee and K. K. Lo, Tuning the organelle specificity and cytotoxicity of iridium(III) photosensitisers for enhanced phototheranostic applications, *Chem. Commun.*, 2021, 57 (90), 12008–12011.
10. K. N. Wang, L. Y. Liu, G. Qi, X. J. Chao, W. Ma, Z. Yu, Q. Pan, Z. W. Mao and B. Liu, Light-driven cascade mitochondria-to-nucleus photosensitization in cancer cell ablation, *Adv. Sci.*, 2021, 8 (8), 2004379.

11. M. M. Wang, F. J. Xu, Y. Su, Y. Geng, X. T. Qian, X. L. Xue, Y. Q. Kong, Z. H. Yu, H. K. Liu and Z. Su, A new strategy to fight metallodrug resistance: mitochondria-relevant treatment through mitophagy to inhibit metabolic adaptations of cancer cells, *Angew. Chem. Int. Ed.*, 2022, 61 (27), e202203843.
12. Q. Y. Yi, D. Wan, B. Tang, Y. J. Wang, W. Y. Zhang, F. Du, M. He and Y. J. Liu, Synthesis, characterization and anticancer activity in vitro and in vivo evaluation of an iridium (III) polypyridyl complex, *Eur. J. Med. Chem.*, 2018, 145 (1), 338–349.
13. H. Yuan, Z. Han, Y. Chen, F. Qi, H. Fang, Z. Guo, S. Zhang and W. He, Ferroptosis photoinduced by new cyclometalated Iridium(III) complexes and its synergism with apoptosis in tumor cell inhibition, *Angew. Chem. Int. Ed.*, 2021, 60 (15), 8174–8181.
14. L. Feng, Y. Geisselbrecht, S. Blanck, A. Wilbuer, G. E. Atilla-Gokcumen, P. Filippakopoulos, K. Kraling, M. A. Celik, K. Harms, J. Maksimoska, R. Marmorstein, G. Frenking, S. Knapp, L. O. Essen and E. Meggers, Structurally sophisticated octahedral metal complexes as highly selective protein kinase inhibitors, *J. Am. Chem. Soc.*, 2011, 133 (15), 5976–5986.
15. L. He, K. Xiong, L. Wang, R. Guan, Y. Chen, L. Ji and H. Chao, Iridium(III) complexes as mitochondrial topoisomerase inhibitors against cisplatin-resistant cancer cells, *Chem. Commun.*, 2021, 57 (67), 8308–8311.
16. R. R. Ye, C. P. Tan, L. He, M. H. Chen, L. N. Ji and Z. W. Mao, Cyclometalated Ir(III) complexes as targeted theranostic anticancer therapeutics: combining HDAC inhibition with photodynamic therapy, *Chem. Commun.*, 2014, 50 (75), 10945–10948.
17. L. J. Liu, L. Lu, H. J. Zhong, B. He, D. W. Kwong, D. L. Ma and C. H. Leung, An iridium(III) complex inhibits JMJD2 activities and acts as a potential epigenetic modulator, *J. Med. Chem.*, 2015, 58 (16), 6697–6703.
18. Q. P. Qin, T. Meng, M. X. Tan, Y. C. Liu, X. J. Luo, B. Q. Zou and H. Liang, Synthesis and in vitro biological evaluation of three 4′-(4-methoxyphenyl)-2,2′:6′,2″-terpyridine iridium(III) complexes as new telomerase inhibitors, *Eur. J. Med. Chem.*, 2018, 143 (1), 1387–1395.
19. A. Zamora, G. Vigueras, V. Rodríguez, M. D. Santana and J. Ruiz, Cyclometalated iridium(III) luminescent complexes in therapy and phototherapy, *Coord. Chem. Rev.*, 2018, 360 (1), 34–76.
20. W. L. Berry and R. Janknecht, KDM4/JMJD2 histone demethylases: epigenetic regulators in cancer cells, *Cancer Res.*, 2013, 73 (10), 2936–2942.
21. L. Fan, S. Xu, F. Zhang, X. Cui, L. Fazli, M. Gleave, D. J. Clark, A. Yang, A. Hussain, F. Rassool and J. Qi, Histone demethylase JMJD1A promotes expression of DNA repair factors and radioresistance of prostate cancer cells, *Cell Death. Dis.*, 2020, 11 (4), 214.
22. Z. Fang, Y. Liu, R. Zhang, Q. Chen, T. Wang, W. Yang, Y. Fan, C. Yu, R. Xiang and S. Yang, Discovery of a potent and selective inhibitor of histone lysine demethylase KDM4D, *Eur. J. Med. Chem.*, 2021, 223 (1), 113662.
23. K. Peng, M. Zhuo, M. Li, Q. Chen, P. Mo and C. Yu, Histone demethylase JMJD2D activates HIF1 signaling pathway via multiple mechanisms to promote colorectal cancer glycolysis and progression, *Oncogene*, 2020, 39 (47), 7076–7091.
24. M. Vinogradova, V. S. Gehling, A. Gustafson, S. Arora, C. A. Tindell, C. Wilson, K. E. Williamson, G. D. Guler, P. Gangurde, W. Manieri, J. Busby, E. M. Flynn, F. Lan, H. J. Kim, S. Odate, A. G. Cochran, Y. Liu, M. Wongchenko, Y. Yang, T. K. Cheung, T. M. Maile, T. Lau, M. Costa, G. V. Hegde, E. Jackson, R. Pitti, D. Arnott, C. Bailey, S. Bellon, R. T. Cummings, B. K. Albrecht, J. C. Harmange, J. R. Kiefer, P. Trojer and M. Classon, An inhibitor of KDM5 demethylases reduces survival of drug-tolerant cancer cells, *Nat. Chem. Biol.*, 2016, 12 (7), 531–538.
25. G. J. Yang, J. Wu, L. Miao, M. H. Zhu, Q. J. Zhou, X. J. Lu, J. F. Lu, C. H. Leung, D. L. Ma and J. Chen, Pharmacological inhibition of KDM5A for cancer treatment, *Eur. J. Med. Chem.*, 2021, 226 (1), 113855.
26. H. U. Kaniskan, M. L. Martini and J. Jin, Inhibitors of protein methyltransferases and demethylases, *Chem. Rev.*, 2018, 118 (3), 989–1068.
27. L. Morera, M. Lubbert and M. Jung, Targeting histone methyltransferases and demethylases in clinical trials for cancer therapy, *Clin. Epigenetics*, 2016, 8 (1), 57.
28. R. A. Varier and H. T. Timmers, Histone lysine methylation and demethylation pathways in cancer, *Biochim. Biophys. Acta*, 2011, 1815 (1), 75–89.
29. T. S. Kang, C. N. Ko, J. T. Zhang, C. Wu, C. Y. Wong, D. L. Ma and C. H. Leung, Rhodium(III)-based inhibitor of the JMJD3-H3K27me3 interaction and modulator of the inflammatory response, *Inorg. Chem.*, 2018, 57 (22), 14023–14026.
30. G. J. Yang, W. Wang, S. W. F. Mok, C. Wu, B. Y. K. Law, X. M. Miao, K. J. Wu, H. J. Zhong, C. Y. Wong, V. K. W. Wong, D. L. Ma and C. H. Leung, Selective inhibition of lysine-specific demethylase 5A (KDM5A) using a rhodium(III) complex for triple-negative breast cancer therapy, *Angew. Chem. Int. Ed.*, 2018, 57 (40), 13091–13095.
31. C. Yang, W. Wang, J. X. Liang, G. Li, K. Vellaisamy, C. Y. Wong, D. L. Ma and C. H. Leung, A Rhodium(III)-based inhibitor of lysine-specific histone demethylase 1 as an epigenetic modulator in prostate cancer cells, *J. Med. Chem.*, 2017, 60 (6), 2597–2603.
32. R. Chen, M. Jaattela and B. Liu, Lysosome as a central hub for rewiring pH homeostasis in tumors, *Cancers*, 2020, 12 (9), 2437.
33. M. Savini, Q. Zhao and M. C. Wang, Lysosomes: signaling hubs for metabolic sensing and longevity, *Trends Cell Biol.*, 2019, 29 (11), 876–887.
34. P. Boya and G. Kroemer, Lysosomal membrane permeabilization in cell death, *Oncogene*, 2008, 27 (50), 6434–6451.
35. L. Galluzzi, J. M. Bravo-San Pedro and G. Kroemer, Organelle-specific initiation of cell death, *Nat. Cell Biol.*, 2014, 16 (8), 728–736.
36. J. Li, Z. Tian, Z. Xu, S. Zhang, Y. Feng, L. Zhang and Z. Liu, Highly potent half-sandwich iridium and ruthenium complexes as lysosome-targeted imaging and anticancer agents, *Dalton Trans.*, 2018, 47 (44), 15772–15782.
37. Z. Xu, J. Huang, D. Kong, Y. Yang, L. Guo, X. Jia, G. Zhong and Z. Liu, Potent half-sandwich Ru(II) N^N (aryl-BIAN) complexes: lysosome-mediated apoptosis, in vitro and in vivo anticancer activities, *Eur. J. Med. Chem.*, 2020, 207 (1), 112763.
38. L. Qiao, J. Liu, Y. Han, F. Wei, X. Liao, C. Zhang, L. Xie, L. Ji and H. Chao, Rational design of a lysosome-targeting and near-infrared absorbing Ru(II)-BODIPY conjugate for photodynamic therapy, *Chem. Commun.*, 2021, 57 (14), 1790–1793.
39. D. Tang, R. Kang, T. V. Berghe, P. Vandenabeele and G. Kroemer, The molecular machinery of regulated cell death, *Cell Res.*, 2019, 29 (5), 347–364.
40. E. Koren and Y. Fuchs, Modes of regulated cell death in cancer, *Cancer Discov.*, 2021, 11 (2), 245–265.
41. B. A. Carneiro and W. S. El-Deiry, Targeting apoptosis in cancer therapy, *Nat. Rev. Clin. Oncol.*, 2020, 17 (7), 395–417.
42. R. W. Johnstone, A. A. Ruefli and S. W. Lowe, Apoptosis: a link between cancer genetics and chemotherapy, *Cell*, 2002, 108 (2), 153–164.
43. F. H. Igney and P. H. Krammer, Death and anti-death: tumour resistance to apoptosis, *Nat. Rev. Cancer*, 2002, 2 (4), 277–288.

44. R. K. Amaravadi, A. C. Kimmelman and J. Debnath, Targeting autophagy in cancer: recent advances and future directions, *Cancer Discov.*, 2019, 9 (9), 1167–1181.
45. V. Nikoletopoulou, M. Markaki, K. Palikaras and N. Tavernarakis, Crosstalk between apoptosis, necrosis and autophagy, *Biochim. Biophys. Acta*, 2013, 1833 (12), 3448–3459.
46. L. He, Z. Y. Pan, W. W. Qin, Y. Li, C. P. Tan and Z. W. Mao, Impairment of the autophagy-related lysosomal degradation pathway by an anticancer rhenium(I) complex, *Dalton Trans.*, 2019, 48 (13), 4398–4404.
47. L. Ke, F. Wei, L. Xie, J. Karges, Y. Chen, L. Ji and H. Chao, A biodegradable iridium(III) coordination polymer for enhanced two-photon photodynamic therapy using an apoptosis-ferroptosis hybrid pathway, *Angew. Chem. Int. Ed.*, 2022, 61(28), e202205429.
48. Y. Yang, Z. Zhou, Z. Z. Wei, Q. P. Qin, L. Yang and H. Liang, High anticancer activity and apoptosis- and autophagy-inducing properties of novel lanthanide(III) complexes bearing 8-hydroxyquinoline-N-oxide and 1,10-phenanthroline, *Dalton Trans.*, 2021, 50 (17), 5828–5834.
49. M. H. Chen, Y. Zheng, X. J. Cai, H. Zhang, F. X. Wang, C. P. Tan, W. H. Chen, L. N. Ji and Z. W. Mao, Inhibition of autophagic flux by cyclometalated iridium(III) complexes through anion transportation, *Chem. Sci.*, 2019, 10 (11), 3315–3323.
50. C. Wu, G. Li, Q. B. Han, R. J. Pei, J. B. Liu, D. L. Ma and C. H. Leung, Real-time detection of oxalyl chloride based on a long-lived iridium(III) probe, *Dalton Trans.*, 2017, 46 (48), 17074–17079.
51. M. S. Islam, T. M. Leissing, R. Chowdhury, R. J. Hopkinson and C. J. Schofield, 2-Oxoglutarate-dependent oxygenases, *Annu. Rev. Biochem.*, 2018, 87 (1), 585–620.
52. Y. Tsukada, J. Fang, H. Erdjument-Bromage, M. E. Warren, C. H. Borchers, P. Tempst and Y. Zhang, Histone demethylation by a family of JmjC domain-containing proteins, *Nature*, 2006, 439 (7078), 811–816.
53. G. J. Anderson and D. M. Frazer, Current understanding of iron homeostasis, *Am. J. Clin. Nutr.*, 2017, 106 (Supplement 6), 1559S–1566S.
54. Z. Fan, J. Xie, T. Sadhukhan, C. Liang, C. Huang, W. Li, T. Li, P. Zhang, S. Banerjee, K. Raghavachari and H. Huang, Highly efficient Ir(III)-coumarin photo-redox catalyst for synergetic multi-mode cancer photo-therapy, *Chem. Eur. J.*, 2022, 28 (3), e202103346.
55. Y. Jiang, F. Li, B. Gao, M. Ma, M. Chen, Y. Wu, W. Zhang, Y. Sun, S. Liu and H. Shen, KDM6B-mediated histone demethylation of LDHA promotes lung metastasis of osteosarcoma, *Theranostics*, 2021, 11 (8), 3868–3881.
56. P. Pandya, J. L. Orgaz and V. Sanz-Moreno, Modes of invasion during tumour dissemination, *Mol. Oncol.*, 2017, 11 (1), 5–27.
57. Y. Wang, X. Yang, M. Yuan, S. Xian, L. Zhang, D. Yang and Y. Cheng, Promotion of ovarian cancer cell invasion, migration and colony formation by the miR21/Wnt/CD44v6 pathway, *Oncol. Rep.*, 2019, 42 (1), 91–102.
58. J. C. Black, A. Allen, C. Van Rechem, E. Forbes, M. Longworth, K. Tschop, C. Rinehart, J. Quiton, R. Walsh, A. Smallwood, N. J. Dyson and J. R. Whetstine, Conserved antagonism between JMJD2A/KDM4A and HP1γ during cell cycle progression, *Mol. Cell*, 2010, 40 (5), 736–748.
59. G. J. Yang, C. N. Ko, H. J. Zhong, C. H. Leung and D. L. Ma, Structure-based discovery of a selective KDM5A inhibitor that exhibits anti-cancer activity via inducing cell cycle arrest and senescence in breast cancer cell lines, *Cancers*, 2019, 11 (1), 92.
60. X. W. Wu, Y. Zheng, F. X. Wang, J. J. Cao, H. Zhang, D. Y. Zhang, C. P. Tan, L. N. Ji and Z. W. Mao, Anticancer Ir(III)-aspirin conjugates for enhanced metabolic immuno-modulation and mitochondrial lifetime imaging, *Chem. Eur. J.*, 2019, 25 (28), 7012–7022.
61. W. Peng, A. M. Hegazy, N. Jiang, X. Chen, H. X. Qi, X. D. Zhao, J. Pu, R. R. Ye and R. T. Li, Identification of two mitochondrial-targeting cyclometalated iridium(III) complexes as potent anti-glioma stem cells agents, *J. Inorg. Biochem.*, 2020, 203 (1), 110909.
62. L. He, Y. Li, C. P. Tan, R. R. Ye, M. H. Chen, J. J. Cao, L. N. Ji and Z. W. Mao, Cyclometalated iridium(III) complexes as lysosome-targeted photodynamic anticancer and real-time tracking agents, *Chem. Sci.*, 2015, 6 (10), 5409–5418.
63. F. X. Wang, M. H. Chen, Y. N. Lin, H. Zhang, C. P. Tan, L. N. Ji and Z. W. Mao, Dual functions of cyclometalated iridium(III) complexes: anti-metastasis and lysosome-damaged photodynamic therapy, *ACS Appl. Mater. Interfaces*, 2017, 9 (49), 42471–42481.
64. M. Mediavilla-Varela, F. J. Pacheco, F. Almaguel, J. Perez, E. Sahakian, T. R. Daniels, L. S. Leoh, A. Padilla, N. R. Wall, M. B. Lilly, M. De Leon and C. A. Casiano, Docetaxel-induced prostate cancer cell death involves concomitant activation of caspase and lysosomal pathways and is attenuated by LEDGF/p75, *Mol. Cancer*, 2009, 8 (1), 68.
65. L. Wang, J. Chang, D. Varghese, M. Dellinger, S. Kumar, A. M. Best, J. Ruiz, R. Bruick, S. Pena-Llopis, J. Xu, D. J. Babinski, D. E. Frantz, R. A. Brekken, A. M. Quinn, A. Simeonov, J. Easmon and E. D. Martinez, A small molecule modulates Jumonji histone demethylase activity and selectively inhibits cancer growth, *Nat. Commun.*, 2013, 4 (1), 2035.
66. N. N. Danial and S. J. Korsmeyer, Cell death: critical control points, *Cell*, 2004, 116 (2), 205–219.
67. K. Segawa and S. Nagata, An apoptotic 'eat me' signal: phosphatidylserine exposure, *Trends Cell Biol.*, 2015, 25 (11), 639–650.
68. R. C. Taylor, S. P. Cullen and S. J. Martin, Apoptosis: controlled demolition at the cellular level, *Nat. Rev. Mol. Cell Biol.*, 2008, 9 (3), 231–241.
69. F. J. Oliver, G. de la Rubia, V. Rolli, M. C. Ruiz-Ruiz, G. de Murcia and J. M. Murcia, Importance of poly(ADP-ribose) polymerase and its cleavage in apoptosis. Lesson from an uncleavable mutant, *J. Biol. Chem.*, 1998, 273 (50), 33533–33539.
70. J. Li and J. Yuan, Caspases in apoptosis and beyond, *Oncogene*, 2008, 27 (48), 6194–6206.
71. Y. Yuan, C. Shi, X. Wu, W. Li, C. Huang, L. Liang, J. Chen, Y. Wang and Y. Liu, Synthesis and anticancer activity in vitro and in vivo evaluation of iridium(III) complexes on mouse melanoma B16 cells, *J. Inorg. Biochem.*, 2022, 232 (1), 111820.
72. R. R. Ye, W. Peng, B. C. Chen, N. Jiang, X. Q. Chen, Z. W. Mao and R. T. Li, Mitochondria-targeted artesunate conjugated cyclometalated iridium(III) complexes as potent anti-HepG2 hepatocellular carcinoma agents, *Metallomics*, 2020, 12 (7), 1131–1141.
73. S. T. Smiley, M. Reers, C. Mottola-Hartshorn, M. Lin, A. Chen, T. W. Smith, G. D. Steele, Jr. and L. B. Chen, Intracellular heterogeneity in mitochondrial membrane potentials revealed by a J-aggregate-forming lipophilic cation JC-1, *Proc. Natl. Acad. Sci.*, 1991, 88 (9), 3671–3675.
74. S. S. Sabharwal and P. T. Schumacker, Mitochondrial ROS in cancer: initiators, amplifiers or an Achilles' heel? *Nat. Rev. Cancer*, 2014, 14 (11), 709–721.
75. C. P. LeBel, H. Ischiropoulos and S. C. Bondy, Evaluation of the probe 2',7'-dichlorofluorescin as an indicator of reactive oxygen species formation and oxidative stress, *Chem. Res. Toxicol.*, 1992, 5 (2), 227–231.
76. I. Tanida, N. Minematsu-Ikeguchi, T. Ueno and E. Kominami, Lysosomal turnover, but not a cellular level, of endoge-

nous LC3 is a marker for autophagy, *Autophagy*, 2005, 1 (2), 84–91.
77. E. White, Deconvoluting the context-dependent role for autophagy in cancer, *Nat. Rev. Cancer*, 2012, 12 (6), 401–410.
78. N. L. Pan, J. X. Liao, M. Y. Huang, Y. Q. Zhang, J. X. Chen, Z. W. Zhang, Z. X. Yang, X. E. Long, X. T. Wu and J. Sun, Lysosome-targeted ruthenium(II) complexes induce both apoptosis and autophagy in HeLa cells, *J. Inorg. Biochem.*, 2022, 229 (1), 111729.
79. A. L. Wang, M. E. Boulton, W. A. D. Jr, H. V. Rao, J. Cai, T. J. Lukas and A. H. Neufeld, Using LC3 to monitor autophagy flux in the retinal pigment epithelium, *Autophagy*, 2009, 5 (8), 1190–1193.
80. J. Zhan, J. He, Y. Zhou, M. Wu, Y. Liu, F. Shang and X. Zhang, Crosstalk between the autophagy-lysosome pathway and the ubiquitin-proteasome pathway in retinal pigment epithelial cells, *Curr. Mol. Med.*, 2016, 16 (5), 487–495.
81. K. A. King and R. J. Watts, Dual emission from an ortho-metalated iridium(III) complex, *J. Am. Chem. Soc.*, 1987, 109 (5), 1589–1590.
82. C. Li, M. Yu, Y. Sun, Y. Wu, C. Huang and F. Li, A nonemissive iridium(III) complex that specifically lights-up the nuclei of living cells, *J. Am. Chem. Soc.*, 2011, 133 (29), 11231–11239.
83. Y. You and S. Y. Park, Inter-ligand energy transfer and related emission change in the cyclometalated heteroleptic iridium complex: facile and efficient color tuning over the whole visible range by the ancillary ligand structure, *J. Am. Chem. Soc.*, 2005, 127 (36), 12438–12439.
84. G. M. Morris, R. Huey, W. Lindstrom, M. F. Sanner, R. K. Belew, D. S. Goodsell and A. J. Olson, AutoDock4 and AutoDockTools4: automated docking with selective receptor flexibility, *J. Comput. Chem.*, 2009, 30 (16), 2785–2791.
85. M. J. McKeage, S. J. BernersPrice, P. Galettis, R. J. Bowen, W. Brouwer, L. Ding, L. Zhuang and B. C. Baguley, Role of lipophilicity in determining cellular uptake and antitumour activity of gold phosphine complexes, *Cancer Chemother. Pharmacol.*, 2000, 46 (5), 343–350.